Enhanced EKF-based Time Calibration for GNSS/UWB Tight Integration

Enhanced EKF-based Time Calibration for GNSS/UWB Tight Integration

Yihan Guo, Oliviero Vouch, *Student Member, IEEE*, Simone Zocca, *Student Member, IEEE*, Alex Minetto, *Member, IEEE* and Fabio Dovis, *Member, IEEE*

***Abstract*— Tight integration of low-cost Ultra-Wide Band (UWB) ranging sensors with mass-market Global Navigation Satellite System (GNSS) receivers is gaining attention as a high-accuracy positioning strategy for consumer applications dealing with challenging environments. However, due to independent clocks embedded in Commercial-Off-The-Shelf (COTS) chipsets, the time scales associated with sensor measurements are misaligned, leading to inconsistent data fusion. Centralized, recursive filtering architectures can compensate for this offset and achieve accurate state estimation. In line with this, a GNSS/UWB tight integration scheme based on an Extended Kalman Filter (EKF) is developed that performs online time calibration of the sensors' measurements by recursively modeling the GNSS/UWB time-offset as an additional unknown in the system state-space model. Furthermore, a double-update filtering model is proposed that embeds optimizations for the adaptive weighting of UWB measurements. Simulation results show that the double-update EKF algorithm can achieve a horizontal positioning accuracy gain of 41.60 % over a plain EKF integration with uncalibrated time-offset and of 15.43 % over the EKF with naive time-offset calibration. Moreover, a real-world experimental assessment demonstrates improved Root-Mean-Square Error (RMSE) performance of 57.58 % and 31.03 %, respectively.**

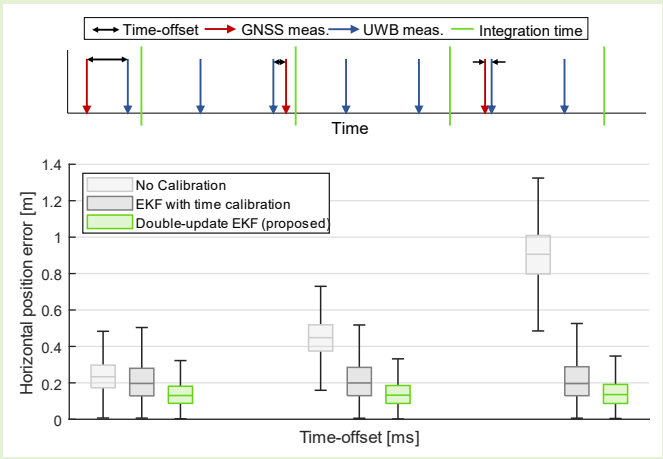

***Index Terms*— Global Navigation Satellite System (GNSS), Extended Kalman Filter (EKF), tight integration, time calibration, Ultra-Wide Band (UWB).**

I. Introduction

NOWADAYS, hundreds of applications in the mass-market segment are pushing the demand for continuous and dependable Positioning, Navigation and Timing (PNT) services, and geo-positioning sensors such as the Global Navigation Satellite System (GNSS) are key enablers to satisfy these growing needs [1], [2]. Whilst different applications often pinpoint diverse requirements, enhanced accuracy and availability of the navigation solution are crucial for reliable positioning and guidance of agents. As a matter of fact, the robustness of the standalone GNSS technology is severely compromised in harsh environments, such as dense urban areas or wooded zones; the interplay between manifold impairing phenomena contribute to degrade the quality of GNSS standalone PNT solutions [3]–[5]. Hence, the design of GNSS-based navigation units in the mass-market segment has been increasingly addressing customizable, embedded architectures integrating low-cost ranging sensors [6], [7].

Latest proliferation in consumer electronics of Ultra-Wide Band (UWB) Impulse Radio (IR) transceivers - featuring small size and low power consumption - makes it an appealing candidate for hybridisation with GNSS signals [8], [9]. As a carrier-free, spread-spectrum communication technology transmitting non-sinusoidal pulses with nanosecond life-cycle, UWB can ensure centimetre-level accurate ranging in dense, cluttered environments thanks to supreme time resolution and remarkable obstacle penetration capabilities [10]. For outdoor applications, on-site deployment of georeferenced UWB beacons - acting as local environment landmarks - can help relative localisation and dynamic tracking of mobile receivers in areas with reduced GNSS availability [11].

Traditional signal processing methods for centralised sensor fusion, such as recursive Maximum a-Posteriori (MAP) filters based on Bayesian estimation algorithms, assume accurately timestamped and synchronised measurements from

Manuscript received Month XX, 2022; revised Month XX, 2022. This work has been supported by the Politecnico di Torino Interdepartmental Centre for Service Robotics PIC4SeR. Y. Guo acknowledges the Chinese Scholarship Council (CSC). A. Minetto acknowledges funding from the research contract no. 32-G-13427-5 DM 1062/2021 funded within the Programma Operativo Nazionale (PON) Ricerca e Innovazione of Italian Ministry of University and Research.

The authors are with the Department of Electronics and Telecommunications (DET), Politecnico di Torino, Turin, Italy. e-mail: (see http://www.navsas.eu).

different sensors to deliver trustworthy state-estimation performance [12], [13]. However, in the framework of low-cost GNSS/UWB tight integration, commercial UWB transceivers and mass-market GNSS chipsets operate as self-contained subsystems carrying independent, asynchronous clocks. Hence, GNSS and UWB measurements are timestamped with respect to different time-scales, and timing disturbances such as latency jitters or spurious clock drifts can affect the timestamping precision with respect to the true sampling instant. Moreover, at each estimation epoch, a lag exists between the measurements' timestamp and the time instant at which the integration filter (also known as hybridisation, or navigation filter) processes the measurements. In particular, this lag is different for GNSS and UWB measurements because sampling rates are different and clocks are independent. Consequently, an unknown time-offset exists between the GNSS observables' timestamps and the UWB measurements' timestamps which models the relative misalignment between the GNSS and UWB time-scales as well as the shift of these scales with respect to the integration filter time-scale [14]. If neglected, this time-offset injects an inconsistency bias into the hybridisation algorithm which may jeopardise state-estimation accuracy [15], [16]. This study aims at proposing a novel time calibration method to guarantee a consistent GNSS/UWB tight integration [12], thus enhancing the benefits introduced by UWB superior ranging accuracy over short distances.

In multisensor systems' literature, different methodologies have been explored to handle synchronisation among self-contained sensor units. On the one hand, hardware-level synchronisation - especially popular in the framework of GNSS-aided strapdown Inertial Navigation System (INS) systems [17], [18] - typically exploits the Pulse-Per-Second (PPS) signal from the GNSS receiver as triggering reference, and it cross-references the timing signals from the coupled sensors in order to establish a shared event base in the integration engine [19], [20]. As a preferred alternative when integrating Commercial Off-The-Shelf (COTS) sensors which feature limited access to the hardware, software-based strategies are put in place; they operate a time calibration process involving accurate time-offset estimation in the integration architecture by leveraging sensors' measurement models [21], [22]. Consequently, software-based solutions can vary significantly depending on the sensors which are taken into account and the associated sensor integration models. In the existing literature, most of the proposed techniques address time calibration as a registration task, where time-offsets are estimated through an offline, pre-processing step. For example, [23]–[25] suggest a continuous-time batch formulation of the time calibration problem, fitting with the framework of maximum likelihood estimation. Moreover, [26], [27] perform visual-inertial time calibration by temporally aligning orientation curves sensed by the independent sensors. Yet joint multisensor optimisation-based calibration strategies are explored in [28], [29]. As opposed to offline techniques, online temporal calibration via filtering-based methods (i.e., filtering-based calibration) is a promising alternative [30], [31]; this strategy models and recursively estimates the time-offset as an additional state-vector unknown under the hybridisation filter state-space formulation [31], [32]. In this paper, filtering-based time calibration is implemented in the context of GNSS/UWB tight integration and, at the time of writing, applications of online GNSS/UWB calibration are still missing in the literature.

After exploring the impact of uncalibrated time-offset on state-estimation performance via plain Extended Kalman Filter (EKF) hybridisation, an EKF-based filtering model supporting time-offset calibration is established for GNSS/UWB tight integration. Nonetheless, the naive EKF-based time calibration model suffers pitfalls that can compromise integration performance under peculiar kinematic conditions [30]. In fact, the local identifiability [33] of the time-offset - i.e., the accurate and unique estimation of such an unknown timing parameter based on the available observables - can be undermined by the relative geometry between the mobile receiver and the UWB nodes, thus leading to an ineffective time calibration. Therefore, a novel, double-update EKF architecture with an optimized weighting of UWB covariance statistics is put forward in order to mitigate the impact of the relative UWB anchors' geometry on accurate time-offset estimation. The proposed double-update EKF model is experimentally assessed to demonstrate the improved positioning accuracy against both plain EKF integration (i.e., without time-offset calibration) and EKF integration with naive time-offset calibration. To this end, after identifying critical kinematic conditions leading to performance deterioration induced by uncalibrated time-offset, experiments with simulated data are carried out over sample vehicular scenarios characterised by considerable variability of the observable processes. In addition, the effectiveness and practicability of the proposed time calibration methodology for GNSS/UWB tight integration are further validated with a real-world assessment for a vehicular trajectory in a suburban area.

The paper outline is organized as follows: Section II lays the mathematical foundations for a discrete-time filtering model fitting with GNSS/UWB tight integration. After that, Section III introduces a convenient GNSS/UWB time-offset formulation and carries out a mathematical analysis to highlight the time-offset propagation on EKF state-estimation error. Then, Section IV, after enhancing the tight integration model for EKF-based time-offset calibration, presents the novel, double-update EKF with adaptive weighting of UWB measurements. Eventually, Section V experimentally quantifies the navigation accuracy degradation caused by plain EKF tight integration and carries out a statistical performance assessment of the proposed calibration methodology both with simulated and real-world data.

II. EKF-based GNSS/UWB Tight Integration

Addressing the problem of recursive estimation of the time-varying state of a dynamic system, along with the continuous flow of noisy observation information, the hybridisation filter builds upon a Discrete-Time System State Space (DSS) formulation. The latter models the dynamic state evolution of the tracked mobile agent and the measurements, jointly with the associated noise statistics [34].

A. GNSS code-based ranging model

In the observation model for GNSS/UWB tight integration, GNSS ranging data include raw pseudorange and Doppler-shift observables. As a matter of fact, pseudorange measurements carry GNSS satellites-to-receiver ranging information corrupted by the contributions of receiver clock bias, atmospheric delay, and other impairments affecting the GNSS Signal-in-Space (SIS) propagation [35]. After compensation of modelled bias components, the pseudorange measurement equation for the i-th GNSS satellite at generic epoch k can be written in metric units as [36]:

$$\rho_{G,k}^{(i)} = \underbrace{\sqrt{(x_{G,k}^{(i)} - r_{x,k})^2 + (y_{G,k}^{(i)} - r_{y,k})^2 + (z_{G,k}^{(i)} - r_{z,k})^2}}_{r_k^{(i)}} + \delta t_{u,k} + \epsilon_{G,k}^{(i)} \quad (1)$$

where:

- $r_k^{(i)}$ is the true, geometric range from satellite i to receiver at epoch k;
- $\boldsymbol{r}_{G,k}^{(i)} = \left(x_{G,k}^{(i)}, y_{G,k}^{(i)}, z_{G,k}^{(i)}\right)$ is the k-th epoch position vector of satellite i expressed in Earth-Centred Earth-Fixed (ECEF) coordinates;
- $\boldsymbol{r}_{u,k} = (r_{x,k}, r_{y,k}, r_{z,k})$ is the k-th epoch receiver position vector expressed in ECEF coordinates;
- $\delta t_{u,k}$ is the receiver clock bias term at epoch k;
- $\epsilon_{G,k}^{(i)}$ is the residual error in the pseudorange measurement from i-th satellite.

Doppler-shift measurements, instead, bring information about the relative dynamics between each GNSS satellite and the receiver; hence, they are relevant to the estimation of both the receiver velocity and the receiver clock drift. By differentiating (1), the Doppler-shift model for the i-th GNSS satellite at generic epoch k can be obtained in terms of satellite-to-receiver range variation rate [36]:

$$\dot{\rho}_{G,k}^{(i)} = \dot{r}_k^{(i)} + \delta f_{u,k} + \dot{\epsilon}_{G,k}^{(i)} \quad (2)$$

where:

- $\dot{\rho}_{G,k}^{(i)}$ is the k-th epoch pseudorange-rate measurement from satellite i;
- $\dot{r}_k^{(i)}$ is the rate of change of the true, geometric range from satellite i to receiver at epoch k;
- $\delta f_{u,k}$ is the receiver clock drift;
- $\dot{\epsilon}_{G,k}^{(i)}$ is the residual error in the pseudorange-rate measurement from i-th satellite.

As a matter of fact, the range-rate $\dot{r}_k^{(i)}$ can be thought as the projection of satellite-to-receiver velocity vector on the transmitter-receiver Line-Of-Sight (LOS) [36]:

$$\dot{r}_k^{(i)} = (\boldsymbol{v}_{G,k}^{(i)} - \boldsymbol{v}_{u,k}) \cdot \boldsymbol{I}_k^{(i)} \quad (3)$$

where:

- $\boldsymbol{v}_{G,k}^{(i)} = \left(\dot{x}_{G,k}^{(i)}, \dot{y}_{G,k}^{(i)}, \dot{z}_{G,k}^{(i)}\right)$ is the k-th epoch velocity vector of satellite i expressed in ECEF coordinates;
- $\boldsymbol{v}_{u,k} = (v_{x,k}, v_{y,k}, v_{z,k})$ is the k-th epoch receiver velocity vector expressed in ECEF coordinates;
- $\boldsymbol{I}_k^{(i)}$ is the k-th epoch LOS unit vector from the receiver position to the i-th satellite position expressed in ECEF coordinates.

Moreover, $\dot{\rho}_{G,k}^{(i)}$ can be also expanded as [36]:

$$\dot{\rho}_{G,k}^{(i)} = -\lambda_c f_{d,k}^{(i)} \quad (4)$$

λ_c being the nominal carrier wavelength of the transmitted SIS and $f_{d,k}^{(i)}$ being the k-th epoch received Doppler-shift from satellite i. It follows that, by substituting (3) and (4) into (2), the Doppler measurement model can be expressed as a function of the unknown receiver velocity and clock-drift states [36]:

$$\underbrace{\dot{\rho}_{G,k}^{(i)} - \boldsymbol{v}_{G,k}^{(i)} \cdot \boldsymbol{I}_k^{(i)}}_{d_{G,k}^{(i)}} = -\boldsymbol{I}_k^{(i)} \cdot \boldsymbol{v}_{u,k} + \delta f_{u,k} + \dot{\epsilon}_{G,k}^{(i)} \quad (5)$$

B. UWB measurement model

UWB leverages time-based protocols to pursue peer-to-peer ranging. Adopting a Time-Of-Arrival (TOA)-based ranging model [37], the baseline UWB ranging equation to the j-th UWB anchor at generic epoch k can be written as:

$$\rho_{U,k}^{(j)} = \sqrt{(x_{U,k}^{(j)} - r_{x,k})^2 + (y_{U,k}^{(j)} - r_{y,k})^2 + (z_{U,k}^{(j)} - r_{z,k})^2} + \epsilon_{U,k}^{(j)} \quad (6)$$

where:

- $\rho_{U,k}^{(j)}$ is the measured two-way range from the receiver to the j-th UWB anchor node;
- $\boldsymbol{r}_{U,k}^{(j)} = \left(x_{U,k}^{(j)}, y_{U,k}^{(j)}, z_{U,k}^{(j)}\right)$ is the k-th epoch position vector of UWB anchor j expressed in ECEF coordinates;
- $\epsilon_{U,k}^{(j)}$ is the residual error due to additive noise, Non-Line-of-sight (NLOS) propagation, and further unmodelled effects [38].

C. GNSS/UWB state-space model

For the GNSS/UWB tight integration architecture under study, a total-state implementation is considered which estimates absolute properties of the system [39], [40]. Under the established framework of a discrete-time, EKF-based MAP tracking filter model [41]–[43], the state-vector at generic epoch k can be defined:

$$\boldsymbol{x}_{u,k} = \begin{bmatrix} \boldsymbol{r}_{u,k} & \boldsymbol{v}_{u,k} & \boldsymbol{a}_{u,k} & \delta t_{u,k} & \delta f_{u,k} \end{bmatrix}^T \quad (7)$$

where $\boldsymbol{a}_{u,k} = (a_{x,k}, a_{y,k}, a_{z,k})$ is the receiver acceleration vector expressed in ECEF coordinates. As proven in Section III, GNSS/UWB time calibration is especially required in high-dynamic scenarios. Therefore, a constant acceleration model [44] is necessary to ensure enough accuracy of the system model to finely track the state-vector evolution.

1) GNSS/UWB system model: The discretisation method of the state-transition function from a continuous-time Linear Time-Invariant (LTI) system is given in [40]. Given a constant acceleration model for state dynamics [44], the state-transition matrix $\boldsymbol{F}_k$ - obtained as the first-order truncation of the power-series expansion of the linearised system matrix about the state-vector estimate - can be written as:

$$\boldsymbol{F}_k = \begin{bmatrix} \boldsymbol{I}_{3\times3} & \boldsymbol{I}_{3\times3}\Delta t & 0.5\boldsymbol{I}_{3\times3}\Delta t^2 & \boldsymbol{0}_{3\times1} & \boldsymbol{0}_{3\times1} \\ \boldsymbol{0}_{3\times3} & \boldsymbol{I}_{3\times3} & \boldsymbol{I}_{3\times3}\Delta t & \boldsymbol{0}_{3\times1} & \boldsymbol{0}_{3\times1} \\ \boldsymbol{0}_{3\times3} & \boldsymbol{0}_{3\times3} & \boldsymbol{I}_{3\times3} & \boldsymbol{0}_{3\times1} & \boldsymbol{0}_{3\times1} \\ \boldsymbol{0}_{1\times3} & \boldsymbol{0}_{1\times3} & \boldsymbol{0}_{1\times3} & 1 & \Delta t \\ \boldsymbol{0}_{1\times3} & \boldsymbol{0}_{1\times3} & \boldsymbol{0}_{1\times3} & 0 & 1 \end{bmatrix} \quad (8)$$

where Δt is the time between consecutive epochs (i.e., the time discretisation step) and $\boldsymbol{I}_{3x3}$ is the third-order identity matrix.

The system (or process) noise covariance matrix $\boldsymbol{Q}_k$ - which can also be obtained from the inference method when discretising the state-transition function [40] - gathers any disturbance in the state characterization [42], and it can be split into two terms. By fixing a Cartesian direction (e.g., x-direction) in the ECEF reference frame, the process noise covariance for the corresponding navigation components $\begin{bmatrix} r_{x,k} & v_{x,k} & a_{x,k} \end{bmatrix}^T$ in (7) can be expressed as:

$$\boldsymbol{Q}_{x,k} = \begin{bmatrix} \frac{1}{20}S_{j_x}\Delta t^5 & \frac{1}{8}S_{j_x}\Delta t^4 & \frac{1}{6}S_{j_x}\Delta t^3 \\ \frac{1}{8}S_{j_x}\Delta t^4 & \frac{1}{3}S_{j_x}\Delta t^3 & \frac{1}{2}S_{j_x}\Delta t^2 \\ \frac{1}{6}S_{j_x}\Delta t^3 & \frac{1}{2}S_{j_x}\Delta t^2 & S_{j_x}\Delta t \end{bmatrix} \tag{9}$$

where S_{j_x} is the Power Spectral Density (PSD) of acceleration noise in the ECEF-frame for x-direction. Specifically, formulation (9) is valid under the assumption that process noise realizations come from a band-limited white noise process as long as the sampling rate is much less than the double-sided process noise bandwidth [40]. Equivalent modelling applies to the other Cartesian directions as well. Similarly, the process noise covariance for the timing parameters $\begin{bmatrix} \delta t_{u,k} & \delta f_{u,k} \end{bmatrix}^T$ in (7) can be written as:

$$\boldsymbol{Q}_{c,k} = \begin{bmatrix} S_t\Delta t + S_f\frac{\Delta t^3}{3} & S_f\frac{\Delta t^2}{2} \\ S_f\frac{\Delta t^2}{2} & S_f\Delta t \end{bmatrix} \tag{10}$$

where S_t and S_f are the PSDs of clock-bias and clock-drift noise, respectively.

2) GNSS/UWB observation model: Moving ahead in the DSS characterisation, the measurement vector for GNSS/UWB tight integration embeds raw GNSS pseudorange and Doppler-shift observables (Section II-A) as well as UWB-based auxiliary ranging information (Section II-B); at epoch k, it can be formulated as:

$$\boldsymbol{y}_k = \begin{bmatrix} \rho_{G,k}^{(1)} & \dots & \rho_{G,k}^{(n)} & d_{G,k}^{(1)} & \dots & d_{G,k}^{(n)} & \rho_{U,k}^{(1)} & \dots & \rho_{U,k}^{(m)} \end{bmatrix}^T \tag{11}$$

where n is the number of tracked GNSS satellites and m is the number of auxiliary UWB anchors. Then, the linearised observation matrix - which models how measurements can affect the dynamic system state and which is determined from the known properties of the system [40] - can be written as:

$$\boldsymbol{H}_k = \begin{bmatrix} \boldsymbol{H}_{n\times 3}^G & \boldsymbol{0}_{n\times 3} & \boldsymbol{1}_{n\times 1} & \boldsymbol{0}_{n\times 1} \\ \boldsymbol{0}_{n\times 3} & \boldsymbol{H}_{n\times 3}^G & \boldsymbol{0}_{n\times 1} & \boldsymbol{1}_{n\times 1} \\ \boldsymbol{H}_{m\times 3}^U & \boldsymbol{0}_{m\times 3} & \boldsymbol{0}_{m\times 1} & \boldsymbol{0}_{m\times 1} \end{bmatrix} \tag{12}$$

In (12), the term $\boldsymbol{H}_{n\times 3}^G$ identifies the Jacobian matrix resulting from first-order linearisation of (1) and (5). It can be written as:

$$\boldsymbol{H}_{n\times 3}^G = \frac{\partial(h_1,\dots,h_n)}{\partial(r_x,r_y,r_z)} = \begin{bmatrix} \frac{-(x_G^{(1)}-r_x)}{r^{(1)}} & \frac{-(y_G^{(1)}-r_y)}{r^{(1)}} & \frac{-(z_G^{(1)}-r_z)}{r^{(1)}} \\ \frac{-(x_G^{(2)}-r_x)}{r^{(2)}} & \frac{-(y_G^{(2)}-r_y)}{r^{(2)}} & \frac{-(z_G^{(2)}-r_z)}{r^{(2)}} \\ \vdots & \vdots & \vdots \\ \frac{-(x_G^{(n)}-r_x)}{r^{(n)}} & \frac{-(y_G^{(n)}-r_y)}{r^{(n)}} & \frac{-(z_G^{(n)}-r_z)}{r^{(n)}} \end{bmatrix} \tag{13}$$

where $r^{(i)}$ is the true geometric range from the receiver to satellite i. In particular, the i-th row of $\boldsymbol{H}_{n\times 3}^G$ collects the Cartesian components of the unit steering vector pointing from the receiver position to the i-th satellite position. Similarly, the term $\boldsymbol{H}_{m\times 3}^U$ is the Jacobian matrix for UWB ranging model (6) and, in row j, it collects the Cartesian components of the unit steering vector from the receiver position to the j-th UWB anchor position. Overall, $\boldsymbol{H}_{m\times 3}^U$ has a similar structure to $\boldsymbol{H}_{n\times 3}^G$.

III. The Impact of Time-Offset on GNSS/UWB Tight Integration Accuracy

In this section, after establishing a mathematical formulation for GNSS/UWB time-offset, a theoretical analysis is carried out to investigate its impact on EKF-based state-estimation.

A. Time-offset definition

As mentioned in Section I, given independent rates and time-scales between the GNSS receiver clock and the UWB transceiver clock, an unknown time-offset exists between the timestamps of raw GNSS observables and the timestamps of auxiliary UWB ranging measurements [31].

At a generic epoch k, the tight integration filter combines GNSS and UWB measurements in the observation model at a time instant t_k tagged to the integration time-scale. Then, two quantities are identified:

- $\delta t_{G,k}$ expresses the unknown lag between the available set of GNSS measurements (timestamped in the GNSS time-scale) and t_k;
- $\delta t_{U,k}$ expresses the unknown lag between the available set of auxiliary UWB measurements (timestamped in the UWB time-scale) and t_k;

Then, the GNSS/UWB time-offset is defined as:

$$t_{d,k} = \delta t_{U,k} - \delta t_{G,k} \tag{14}$$

which expresses the misalignment of the timestamp associated to the set of auxiliary UWB measurements (tagged to the UWB time-scale) with respect to the GNSS time-scale. The time-offset $t_{d,k}$ includes the shift - under the GNSS time-scale - between the timestamping times of GNSS and UWB measurements and it can can be either a positive or a negative quantity at any epoch.

As a matter of fact, $t_{d,k}$ accounts for two time-varying effects:

- the relative misalignment between the GNSS and UWB measurements because of the different sampling rates and clocks of the independent sensors;
- the lag of GNSS and UWB time-scales with respect to the time-scale of the centralized processing unit running the GNSS/UWB tight integration algorithm.

While the former effect embeds non-idealities of individual sensor clocks (e.g., clock drift and latency jitters), the latter effect is contributed by manifold sources such as data-transfer latencies, hardware-level processing and software overhead in the centralised processing unit. Furthermore, under the assumption of high UWB sampling rate and small drift of

sensor clocks, $t_{d,k}$ can be modelled as a constant between consecutive estimation epochs. Hence, the GNSS/UWB time-offset prediction at epoch k matches with the a-posteriori time-offset update at previous epoch.

A graphical interpretation of the described framework is provided in Fig. 1. The three subplots are referred to a common time-scale, i.e. the integration time-scale. The top and middle subplots show the instants at which GNSS and UWB measurements are dumped, respectively. The bottom subplot shows which measurements the integration filter is processing. In case the measurements were provided at high rate from at least one of the sensors, and the integration took place at a time t_k at which the low-rate measurements are available, this time-offset would be negligible. However, in this work, the aim is to directly estimate $t_{d,k}$ as part of the system state, hence proposing a low-complexity strategy which relaxes constraints on measurements rates or related assumptions.

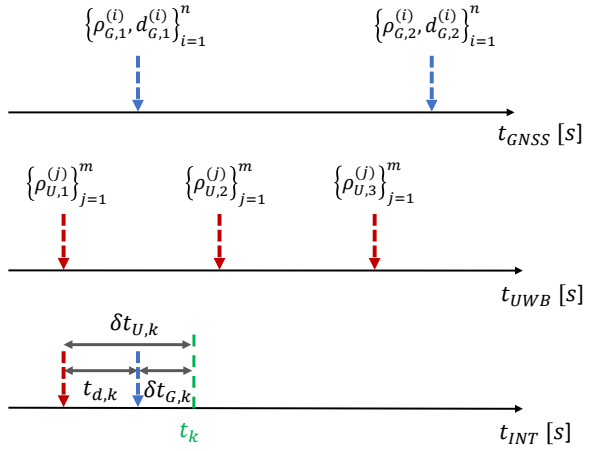

Fig. 1: Diagram of the time-offset between GNSS and UWB measurements involved in a GNSS/UWB tight integration scheme. For readability, GNSS and UWB time axis are assumed aligned to the integration time axis (bottom).

B. Mathematical Analysis

In light of the framework discussed in Section III-A, the GNSS/UWB measurement vector (11) collects observables which are not temporally consistent. In fact, at t_k, the set of available GNSS ranging observables $\left\{\rho_{G,k}^{(i)}\right\}_{i=1}^{n}$ carry information about the mobile user position $\boldsymbol{r}_{u,k}^{G} = \left(r_{x,k}^{G}, r_{y,k}^{G}, r_{z,k}^{G}\right)$ at a time instant which lags t_k by $\delta t_{G,k}$. Conversely, the available set of auxiliary UWB ranges $\left\{\rho_{U,k}^{(j)}\right\}_{j=1}^{m}$ bring information about the mobile user position $\boldsymbol{r}_{u,k}^{U} = \left(r_{x,k}^{U}, r_{y,k}^{U}, r_{z,k}^{U}\right)$ at a time instant which lags t_k by $\delta t_{U,k}$. Therefore, according to (14), $\left\{\rho_{U,k}^{(j)}\right\}_{j=1}^{m}$ is not time-aligned with $\left\{\rho_{G,k}^{(i)}\right\}_{i=1}^{n}$.

Focusing on the auxiliary range to the j-th UWB anchor, (6) can be reframed as:

$$\rho_{U,k}^{(j)} = \sqrt{(x_{U,k}^{(j)} - r_{x,k}^{U})^2 + (y_{U,k}^{(j)} - r_{y,k}^{U})^2 + (z_{U,k}^{(j)} - r_{z,k}^{U})^2} \tag{15}$$

which clearly highlights the mapping onto $\boldsymbol{r}_{u,k}^{U}$. For ease of analysis, the residual error term, $\epsilon_{U,k}^{(j)}$, is neglected hereafter. Leveraging a continuous-time motion model for state dynamics [45], $\boldsymbol{r}_{u,k}^{G}$ can be related to $\boldsymbol{r}_{u,k}^{U}$ as follows:

$$\begin{bmatrix} r_{x,k}^{G} \\ r_{y,k}^{G} \\ r_{z,k}^{G} \end{bmatrix} = \begin{bmatrix} r_{x,k}^{U} + \int_{t_k+\delta t_{U,k}}^{t_k+\delta t_{U,k}-t_{d,k}} v_x(t)dt \\ r_{y,k}^{U} + \int_{t_k+\delta t_{U,k}}^{t_k+\delta t_{U,k}-t_{d,k}} v_y(t)dt \\ r_{z,k}^{U} + \int_{t_k+\delta t_{U,k}}^{t_k+\delta t_{U,k}-t_{d,k}} v_z(t)dt \end{bmatrix} = \begin{bmatrix} r_{x,k}^{U} \\ r_{y,k}^{U} \\ r_{z,k}^{U} \end{bmatrix} + \begin{bmatrix} \varepsilon_{r_x,k} \\ \varepsilon_{r_y,k} \\ \varepsilon_{r_z,k} \end{bmatrix} = \boldsymbol{r}_{u,k}^{U} + \boldsymbol{\epsilon}_{r,k} \tag{16}$$

where $\boldsymbol{v}_u(t) = (v_x(t), v_y(t), v_z(t))$ expresses the instantaneous speed of the receiver and $\boldsymbol{\epsilon}_{r,k}$ identifies the displacement vector along the mobile user trajectory induced by $t_{d,k}$. Given (16), the UWB range to the j-th UWB anchor time-aligned to the available GNSS ranging observables (i.e., lagging t_k by $\delta t_{G,k}$) can be expressed as:

$$\rho_{U,k}^{(j)'} = \sqrt{(x_{U,k}^{(j)} - \underbrace{(r_{x,k}^{U} + \varepsilon_{r_x,k})}_{r_{x,k}^{G}})^2 + (y_{U,k}^{(j)} - \underbrace{(r_{y,k}^{U} + \varepsilon_{r_y,k})}_{r_{y,k}^{G}})^2 + (z_{U,k}^{(j)} - \underbrace{(r_{z,k}^{U} + \varepsilon_{r_z,k})}_{r_{z,k}^{G}})^2} \tag{17}$$

Hence, a UWB ranging error term caused by $t_{d,k}$ can be introduced:

$$\epsilon_{\rho,U,k}^{(j)} = \rho_{U,k}^{(j)'} - \rho_{U,k}^{(j)} = \frac{\left(\rho_{U,k}^{(j)'}\right)^2 - \left(\rho_{U,k}^{(j)}\right)^2}{\rho_{U,k}^{(j)'} + \rho_{U,k}^{(j)}} \tag{18}$$

Substituting (17) and (15) at the numerator of (18), the following expression is obtained:

$$\epsilon_{\rho,U,k}^{(j)} = \frac{\|\boldsymbol{\epsilon}_{r,k}\|^2 - 2(\boldsymbol{r}_{U,k}^{(j)} - \boldsymbol{r}_{u,k}^{U}) \cdot \boldsymbol{\epsilon}_{r,k}}{\rho_{U,k}^{(j)'} + \rho_{U,k}^{(j)}} \tag{19}$$

which shows that, except for a positive scaling factor at the denominator, $\epsilon_{\rho,U,k}^{(j)}$ depends on two terms:

1) the squared length of the position displacement (i.e., the squared norm of $\boldsymbol{\epsilon}_{r,k}$) induced by $t_{d,k}$;
2) a term which is proportional to the length of the projection of $\boldsymbol{\epsilon}_{r,k}$ onto the LOS to the j-th UWB anchor position $\boldsymbol{r}_{U,k}^{(j)}$.

By manipulating (18), $\epsilon_{\rho,U,k}^{(j)}$ for each of the m UWB anchors can be seen as an additive term to the set of auxiliary UWB range measurements. Consequently, it is possible to rewrite (11) as:

$$\boldsymbol{y}_k = \begin{bmatrix} \rho_{G,k}^{(1)} \\ \vdots \\ \rho_{G,k}^{(n)} \\ d_{G,k}^{(1)} \\ \vdots \\ d_{G,k}^{(n)} \\ \rho_{U,k}^{(1)} \\ \vdots \\ \rho_{U,k}^{(m)} \end{bmatrix} = \begin{bmatrix} \rho_{G,k}^{(1)} \\ \vdots \\ \rho_{G,k}^{(n)} \\ d_{G,k}^{(1)} \\ \vdots \\ d_{G,k}^{(n)} \\ \rho_{U,k}^{(1)'} \\ \vdots \\ \rho_{U,k}^{(m)'} \end{bmatrix} - \begin{bmatrix} 0 \\ \vdots \\ 0 \\ 0 \\ \vdots \\ 0 \\ \epsilon_{\rho,U,k}^{(1)} \\ \vdots \\ \epsilon_{\rho,U,k}^{(m)} \end{bmatrix} = \boldsymbol{y}_k' - \boldsymbol{\epsilon}_{\rho,U,k} \tag{20}$$

where $\boldsymbol{y}_k'$ collects time-aligned GNSS and UWB ranging observables. From (20), it is clear that $t_{d,k}$ introduces an

additive error factor $\boldsymbol{\epsilon}_{\rho,U,k}$ in the GNSS/UWB observation model. This error then propagates on the a-posteriori state-estimation error delivered by the tight integration filter.

The EKF innovation vector [41] can be written as:

$$\tilde{\boldsymbol{y}}_k = \boldsymbol{y}_k - h(\hat{\boldsymbol{x}}_{u,k}^-) \tag{21}$$

where $\hat{\boldsymbol{x}}_{u,k}^-$ is the EKF a-priori state-estimate (i.e., the predicted state) at epoch k [41]. By expanding (21) according to (20), the EKF a-posteriori state-estimate (i.e., the updated state) at epoch k [41] is obtained as:

$$\hat{\boldsymbol{x}}_{u,k}^+ = \hat{\boldsymbol{x}}_{u,k}^- + \boldsymbol{K}_k \left(\underbrace{\boldsymbol{y}_k^{'} - \boldsymbol{\epsilon}_{\rho,U,k}}_{\boldsymbol{y}_k} - h\left(\hat{\boldsymbol{x}}_{u,k}^-\right) \right) \tag{22}$$

$\boldsymbol{K}_k$ being the Kalman gain [41], [42] and $\boldsymbol{\epsilon}_{\rho,U,k}$ being the k-th epoch UWB ranging error term.

Eventually, the a-posteriori state-estimation error due to $t_{d,k}$ can be obtained from (22) as:

$$\boldsymbol{\epsilon}_{\rho,\boldsymbol{x},k} = \hat{\boldsymbol{x}}_{u,k}^{+'} - \hat{\boldsymbol{x}}_{u,k}^+ = \boldsymbol{K}_k \boldsymbol{\epsilon}_{\rho,U,k} \tag{23}$$

where $\hat{\boldsymbol{x}}_{u,k}^{+'}$ and $\hat{\boldsymbol{x}}_{u,k}^+$ are the a-posteriori state-estimates obtained using $\boldsymbol{y}_k^{'}$ and $\boldsymbol{y}_k$, respectively.

Analysing (23), both $\boldsymbol{K}_k$ and $\boldsymbol{\epsilon}_{\rho,U,k}$ contribute to introduce errors in the integrated navigation solution. In particular, $\boldsymbol{K}_k$ amplifies the UWB ranging error propagation on the a-posteriori state-estimation. In fact, when $\boldsymbol{K}_k$ converges to an all-zeros matrix - a condition signalling that the EKF is trusting more the state-prediction than sensors' observation information - the impact of $\boldsymbol{\epsilon}_{\rho,U,k}$ is largely mitigated. On the contrary, the state-estimation performance degradation due to $t_{d,k}$ exacerbates when the integration filter puts very high confidence on the observables' set. Moreover, according to (19), the components of $\boldsymbol{\epsilon}_{\rho,U,k}$ depend upon $\boldsymbol{\epsilon}_{r,k}$ which, in turn, is function of $\boldsymbol{v}_u(t)$ according to (16). Therefore, when the components of $\boldsymbol{v}_u(t)$ take small values, the a-posteriori state-estimation error contributed by $t_{d,k}$ reduces accordingly. Oppositely, $\boldsymbol{\epsilon}_{\rho,\boldsymbol{x},k}$ is expected to grow in high dynamics.

IV. Enhanced EKF-based time-offset calibration with double-update filtering

From the analysis presented in Section III-B, $t_{d,k}$ can affect the state-estimation performance as the tight integration filter processes observables which are not time-consistent. Hence, the baseline GNSS/UWB tight integration model of Section II is first improved in order to enable time calibration via EKF architecture. Then, a novel, double-update EKF filtering framework is put forward which enhances time calibration accuracy by adaptively accounting for the local identifiability of $t_{d,k}$ over consecutive epochs [33].

A. Improved GNSS/UWB model for EKF-based time-offset calibration

An extended state-vector is defined at epoch k:

$$\boldsymbol{x}_{u,k} = \begin{bmatrix} \boldsymbol{r}_{u,k} & \boldsymbol{v}_{u,k} & \boldsymbol{a}_{u,k} & \delta t_{u,k} & \delta f_{u,k} & t_{d,k} \end{bmatrix}^T \tag{24}$$

where, compared to (7), the time-offset $t_{d,k}$ is introduced.

Based on (24), and by re-applying linearisation of the process function about the state-vector estimate and discretisation [42], the state-transition matrix modifies as:

$$\boldsymbol{F}_k = \begin{bmatrix} \boldsymbol{I}_{3\times3} & \boldsymbol{I}_{3\times3}\Delta t & 0.5\boldsymbol{I}_{3\times3}\Delta t^2 & \boldsymbol{0}_{3\times1} & \boldsymbol{0}_{3\times1} & \boldsymbol{0}_{3\times1} \\ \boldsymbol{0}_{3\times3} & \boldsymbol{I}_{3\times3} & \boldsymbol{I}_{3\times3}\Delta t & \boldsymbol{0}_{3\times1} & \boldsymbol{0}_{3\times1} & \boldsymbol{0}_{3\times1} \\ \boldsymbol{0}_{3\times3} & \boldsymbol{0}_{3\times3} & \boldsymbol{I}_{3\times3} & \boldsymbol{0}_{3\times1} & \boldsymbol{0}_{3\times1} & \boldsymbol{0}_{3\times1} \\ \boldsymbol{0}_{1\times3} & \boldsymbol{0}_{1\times3} & \boldsymbol{0}_{1\times3} & 1 & \Delta t & 0 \\ \boldsymbol{0}_{1\times3} & \boldsymbol{0}_{1\times3} & \boldsymbol{0}_{1\times3} & 0 & 1 & 0 \\ \boldsymbol{0}_{1\times3} & \boldsymbol{0}_{1\times3} & \boldsymbol{0}_{1\times3} & 0 & 0 & 1 \end{bmatrix} \tag{25}$$

Using (25) in order to approximate the integral involved in the computation of $\boldsymbol{\epsilon}_{r,k}$ based on (16), (15) can be rewritten as:

$$\rho_{U,k}^{(j)} = \sqrt{\begin{aligned}&(x_{U,k}^{(j)} - (r_{x,k}^G - v_{x,k}t_{d,k} - 0.5a_{x,k}t_{d,k}^2))^2 \\ &+(y_{U,k}^{(j)} - (r_{y,k}^G - v_{y,k}t_{d,k} - 0.5a_{y,k}t_{d,k}^2))^2 \\ &+(z_{U,k}^{(j)} - (r_{z,k}^G - v_{z,k}t_{d,k} - 0.5a_{z,k}t_{d,k}^2))^2\end{aligned}} \tag{26}$$

which defines an improved UWB measurement model embedding $t_{d,k}$. Examining (26), the receiver position information brought about by auxiliary UWB ranges (i.e., $\boldsymbol{r}_{u,k}^U$) gets compensated for the displacement locally induced by $t_{d,k}$ in order to geometrically match with the receiver position mapped by raw GNSS observables (i.e., $\boldsymbol{r}_{u,k}^G$). Moreover, the proposed modelling takes $\boldsymbol{r}_{u,k}^G$ as the unknown receiver position in the GNSS/UWB state-space formulation. Therefore, $\boldsymbol{r}_{u,k}^G$ matches with $\boldsymbol{r}_{u,k}$ in (24) at every epoch. Further, based on (26), modifications are required in the Jacobian matrix for UWB ranging $\boldsymbol{H}_{m\times3}^U$, assuming m UWB anchors [8].

B. Double-update filtering with adaptive optimisation

Comparing (26) against (15), the receiver position mapped by $\rho_{U,k}^{(j)}$ is moved along the dynamic model using a specific, yet unknown, value of $t_{d,k}$. Hence, the integration filter can exploit the DSS characterisation to detect the unknown $t_{d,k}$ at t_k based on the difference between $\rho_{U,k}^{(j)'}$ and $\rho_{U,k}^{(j)}$.

For the j-th UWB anchor, a function of the unknown state $t_{d,k}$ can be introduced:

$$f^{(j)}(t_{d,k}) = \rho_{U,k}^{(j)'2} - \rho_{U,k}^{(j)\,2} = (\rho_{U,k}^{(j)'} - \rho_{U,k}^{(j)})(\rho_{U,k}^{(j)'} + \rho_{U,k}^{(j)}) \tag{27}$$

which, by its definition, is proportional to the difference between $\rho_{U,k}^{(j)'}$ and $\rho_{U,k}^{(j)}$, except for a positive amplifying factor $\rho_{U,k}^{(j)'} + \rho_{U,k}^{(j)}$. Given that, after a rough calibration of UWB transceiver clock [46], $t_{d,k}$ takes values of few tens of milliseconds, (27) can be expanded by substitution of (26) and (17) and a first-order approximation applies:

$$f^{(j)}(t_{d,k}) = 2t_{d,k}(\boldsymbol{r}_{U,k}^{(j)} - \boldsymbol{r}_{u,k}^G) \cdot \boldsymbol{v}_{u,k} \tag{28}$$

Apparently, $f^{(j)}(t_{d,k})$ is a function that can drive the quality of $t_{d,k}$ estimation at t_k. In fact, the sharper the envelope of $f^{(j)}(t_{d,k})$ is, the more $t_{d,k}$ can be accurately and uniquely inferred from the set of available observables. Conversely, in case the first-order derivative of $f^{(j)}(t_{d,k})$ approached a null value for some interval in the support, $t_{d,k}$ estimation would be jeopardised. By differentiating (28), it is obtained:

$$\frac{df^{(j)}(t_{d,k})}{dt_{d,k}} \propto \underbrace{(\boldsymbol{r}_{U,k}^{(j)} - \boldsymbol{r}_{u,k}^G)}_{\boldsymbol{h}_{U,k}^{(j)}} \cdot \boldsymbol{v}_{u,k} \tag{29}$$

which highlights that, the smaller is the inner product between the receiver velocity vector $\boldsymbol{v}_{u,k}$ and the steering vector to the j-th UWB anchor location $\boldsymbol{h}_{U,k}^{(j)}$, the weaker is the local identifiability characterising $t_{d,k}$. This is equivalent to say that the auxiliary UWB ranging observable associated to the j-th UWB anchor brings little, if any, information to the integration filter to support accurate $t_{d,k}$ estimation. Fig. 2 displays the addressed geometrical framework. Moreover, when the inner product $\boldsymbol{h}_{U,k}^{(j)} \cdot \boldsymbol{v}_{u,k}$ is small, $t_{d,k}$ would not even cause a significant mismatch between $\rho_{U,k}^{(j)}$ and $\rho_{U,k}^{(j)'}$. As a result, $f^{(j)}(t_{d,k})$ would have little bearing on $t_{d,k}$ estimation.

To cope with the aforementioned phenomenon, the covariance statistics of auxiliary UWB ranging measurements are adaptively weighted in the observation model for GNSS/UWB tight integration. Formally, accounting for the EKF measurement noise covariance matrix $\boldsymbol{R}_k$ [41], the estimated variance of the auxiliary UWB range associated to the j-th UWB anchor is amplified through the following epoch-dependent coefficient:

$$A_k^{(j)} = 1 + C_k \sqrt{1 - \left(\frac{\boldsymbol{h}_{U,k}^{(j)} \cdot \boldsymbol{v}_{u,k}}{\left\| \boldsymbol{h}_{U,k}^{(j)} \right\| \left\| \boldsymbol{v}_{u,k} \right\|} \right)^2} \tag{30}$$

where C_k is an empirically set scaling parameter to rectify the instantaneous amplification effect of geometry on R_k statistics. Focusing on the ranging contribution from j-th UWB anchor, (30) aims at weighting the degree of trust the integration filter should put on $\rho_{U,k}^{(j)}$ to correct the a-priori prediction of $t_{d,k}$ according to the identifiability conditions driven by the geometry-dependent behaviour of (29). In particular, the smaller the sine of the angle between $\boldsymbol{h}_{U,k}^{(j)}$ and $\boldsymbol{v}_{u,k}$ (i.e., the stronger the local identifiability of $t_{d,k}$ based on $\rho_{U,k}^{(j)}$), the smaller the value of the weighting coefficient $A_k^{(j)}$. Hence, the corresponding covariance term modelling the error of $\rho_{U,k}^{(j)}$ would be smaller in order to enhance the contribution of such auxiliary range to the update of $t_{d,k}$. Conversely, the larger the sine of the angle between $\boldsymbol{h}_{U,k}^{(j)}$ and $\boldsymbol{v}_{u,k}$ (i.e., the weaker the local identifiability of $t_{d,k}$ based on $\rho_{U,k}^{(j)}$), the larger the value of $A_k^{(j)}$. In such a case, $\rho_{U,k}^{(j)}$ is poorly informative to perform the update of $t_{d,k}$ and its variance should be enhanced.

Nevertheless, according to Section IV-A, the adaptive weighting of UWB covariance statistics is expected to affect the a-posteriori correction of all state variables in (24), not just $t_{d,k}$. On this matter, it is essential to remark that, by its technological properties, UWB is able to deliver high-accuracy auxiliary ranging information [47]–[49] which can significantly contribute to the update of the navigation states in (24). It follows that the discussed weighting strategy must not affect the a-posteriori estimation of these states given that (30) always operates an amplification of UWB ranging observables' variance. In light of the foregoing, a double-update EKF architecture is developed which marginalises the adaptive weighting on UWB covariance statistics to the a-posteriori update of $t_{d,k}$. For the remainder states in (24), instead, $\boldsymbol{R}_k$ statistics are estimated by leveraging functional relationships with the available measurements [50]. The simplified block scheme in Fig. 3 illustrates the main stages of the proposed double-update model with embedded optimisations.

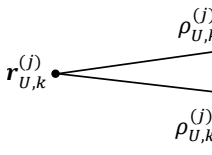

Fig. 2: Example of a scenario characterised by small inner product between the receiver velocity $\boldsymbol{v}_{u,k}$ and the steering vector $\boldsymbol{h}_{U,k}^{(j)}$ to the j-th UWB anchor.

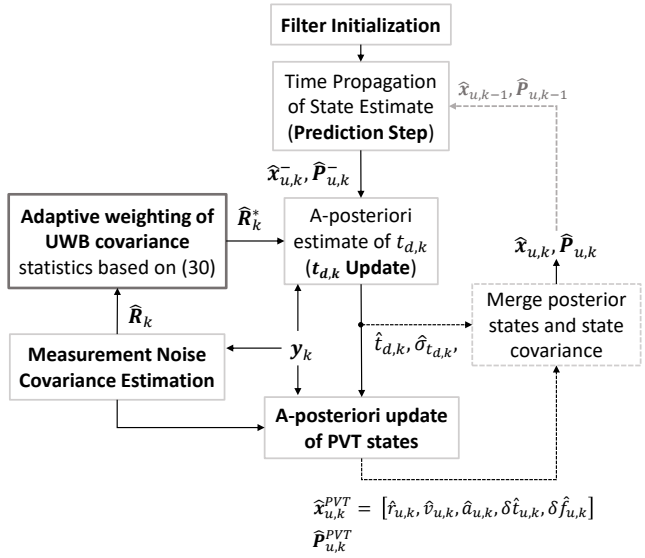

Fig. 3: Processing stages of the double-update EKF architecture with adaptive weighting of UWB covariance statistics for the enhanced calibration of $t_{d,k}$. The input measurement vector $\boldsymbol{y}_k$ is highlighted.

V. Results Analysis

In this section, experiments are presented to assess and validate both the theoretical analysis and the proposed time calibration methodology. In particular, Section V-B simulates the impact of uncalibrated t_d under varying receiver kinematics when leveraging plain EKF tight integration. Then, the following Sections V-C, IV-B compare the simulated and real-world accuracy performance of the double-update EKF architecture against both the EKF model with naive t_d calibration and the plain EKF hybridisation. For ease of notation, the discrete-time index k is omitted henceforth.

A. Experimental set-up and methodology

To pursue the forthcoming assessment, sample vehicular scenarios are first generated through a Radio Frequency (RF) GNSS simulator - IFEN® Network Constellation Simulator (NCS) Titan - in view of extracting the reference trajectory for the simulated vehicular target with a high position update rate of 250 Hz (i.e., 4 ms). The simulated trajectory - the

Bernoullian Lemniscate - is centered in a location specified by its ellipsoidal World Geodetic System 1984 (WGS84) coordinates (Latitude $45.063\,981°$, Longitude $7.659\,017°$) with an horizontal extension of $100\,\mathrm{m}$. From the trajectory center, a network of three static UWB anchors are displaced at a fixed distance of $20\,\mathrm{m}$ and to an height of $5\,\mathrm{m}$ (measured along the vertical direction after taking local tangent plane approximation in correspondence of the trajectory center). A snapshot of the considered scenario is provided in Fig. 4a. For sake of rigorousness, it is remarked that the anchors' placement has been chosen with the sole purpose of establishing a uniform geometric distribution around the Lemniscate centre. Nevertheless, despite out of the scope of this study and left to future investigations, the geometry of the UWB network must be carefully taken into account since the relative localisation estimates' accuracy at each time instant strongly depends on the local position of the mobile target with respect to the auxiliary UWB nodes [51]. Finally, the simulated Global Positioning System (GPS) constellation with the motion track of the satellites is given in Fig. 4b; an elevation mask of $15°$ is used in order to prevent GNSS-based positioning performance deterioration from low-elevation satellites [36].

Based on the addressed scenario, simulations are run by configuring multiple receiver average speeds: $1\,\mathrm{m/s}$, $2\,\mathrm{m/s}$, $5\,\mathrm{m/s}$, $10\,\mathrm{m/s}$, $15\,\mathrm{m/s}$, and $20\,\mathrm{m/s}$. Over the different simulations, a shared time-span with a total duration of 3102 epochs is preserved to guarantee consistency in the comparison of the output results at different target speeds. Raw GNSS observables are logged via the NCS unit for GPS L1 C/A signals at $10\,\mathrm{Hz}$ rate (i.e., $100\,\mathrm{ms}$) in RINEX format. To prevent from idealities, ionospheric effects are modeled inside the GNSS simulator. Logging of ephemeris data is also allowed by the NCS. On the UWB side, for each $250\,\mathrm{Hz}$ position fix in the ground-truth, high-accuracy ranging data to the three UWB anchors are synthetically constructed by leveraging an empirical model proposed in [52], which has been preliminary tested and validated in order to pursue the scopes of this research. Following this approach, UWB datasets with intentional t_d have been constructed. The empirical parameter C_k in (30) is set to 1 after some tests. Finally, by accounting for the GNSS/UWB tight integration framework treated in Section II, a C-language software implementing the EKF-based filtering architectures presented in this paper is run in post-processing on the retrieved datasets. For sake of completeness, Table I specifies relevant settings for matrix $\boldsymbol{Q}_k$ used in the post-processing software and common to all integration architectures. Moreover, the measurement covariance $\boldsymbol{R}_k$ is constructed based on [50] and leveraging the synthetic UWB model [52]. Eventually, state-space domain initialisation for the involved filters is obtained from a Weighted Least-Squares (WLS) positioning solution [35].

B. Impact of uncalibrated t_d on positioning accuracy under varying receiver kinematics

The purpose of such analysis is to build a positioning error map which, depending on the mobile receiver kinematics and on the application-dependent accuracy performance

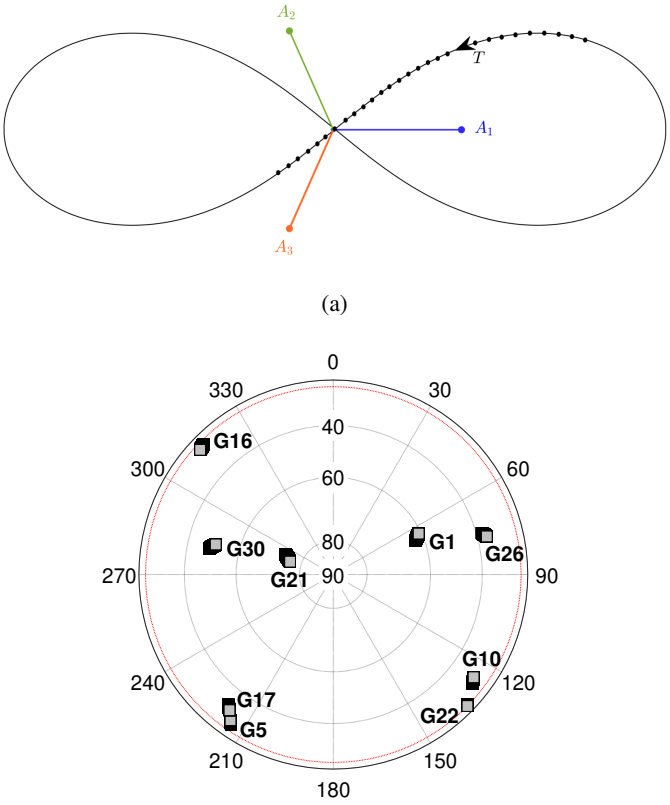

Fig. 4: Experimental scenario. Simulated Bernoullian trajectory travelled by the vehicular target T with three static UWB anchors of opportunity (a). Sky-plot diagram of the simulated GPS constellation. The red dashed line in the elevation grid highlights the cutoff elevation angle (b).

TABLE I: Parameter configuration for process noise covariance matrix $\boldsymbol{Q}_k$ used in the GNSS/UWB tight integration post-processing software.

Parameter	Value	Physical meaning
$S_{j,x}\ S_{j,y}\ S_{j,z}$	$0.4\,\mathrm{m^2/s^5}$	PSD of acceleration noise
S_t	$36\,\mathrm{s}$	PSD of clock bias noise
S_f	$0.01\,\mathrm{s^3}$	PSD of clock drift noise
S_{d_t}	$0.01\,\mathrm{s}$	PSD of time-offset noise

requirements, can suggest whether it is worth or not implementing t_d calibration for GNSS/UWB tight integration. To this end, given the sample vehicular scenarios at different average speeds (Section V-A), synthetic UWB ranging datasets affected by diverse nominal t_d's are processed.

Fig. 5 shows a heatmap chart of the positioning Root-Mean-Square Error (RMSE) for horizontal and vertical directions, respectively. Moreover, the line charts in Fig. 6 highlight both the horizontal and the vertical RMSE patterns over varying t_d, and are parameterised by different average receiver speeds. The positioning RMSE positively correlates with both receiver

speed and t_d, especially when accounting for the horizontal component (the upper plot of Fig. 6). More precisely, for t_d values smaller than $10\,\mathrm{ms}$, the measured RMSE is almost unaffected by the receiver kinematics. However, above $10\,\mathrm{ms}$, it exhibits a nearly exponential increase with the average receiver speed. Looking at the overall horizontal RMSE pattern for small receiver speeds, the increase is nearly linear with t_d, and this agrees with the mathematical analysis carried out in Section III-B. At a given estimation epoch, $\boldsymbol{K}_k$ is mostly the same for different t_d values. Besides, under low kinematics, the receiver speed can be considered constant over a time-span equal to t_d (which is of the order of tens of milliseconds). As a result, recalling (23), $\boldsymbol{\epsilon}_{\rho,U,k}$ and $\boldsymbol{\epsilon}_{\rho,\boldsymbol{x},k}$ increase proportionally with varying t_d following a linear relationship. On the contrary, under higher kinematics, the receiver speed can not be considered constant any more due to the larger instantaneous acceleration. Therefore, the RMSE would not prompt a fixed slope anymore.

Concerning the vertical direction, instead, the RMSE pattern is apparently less regular. Overall, it grows for increasing t_d, but it flattens off as low receiver kinematics are considered. Furthermore, the vertical RMSE statistics are further penalised by the UWB anchors' geometry, and they fluctuate with speed in low kinematic conditions as well.

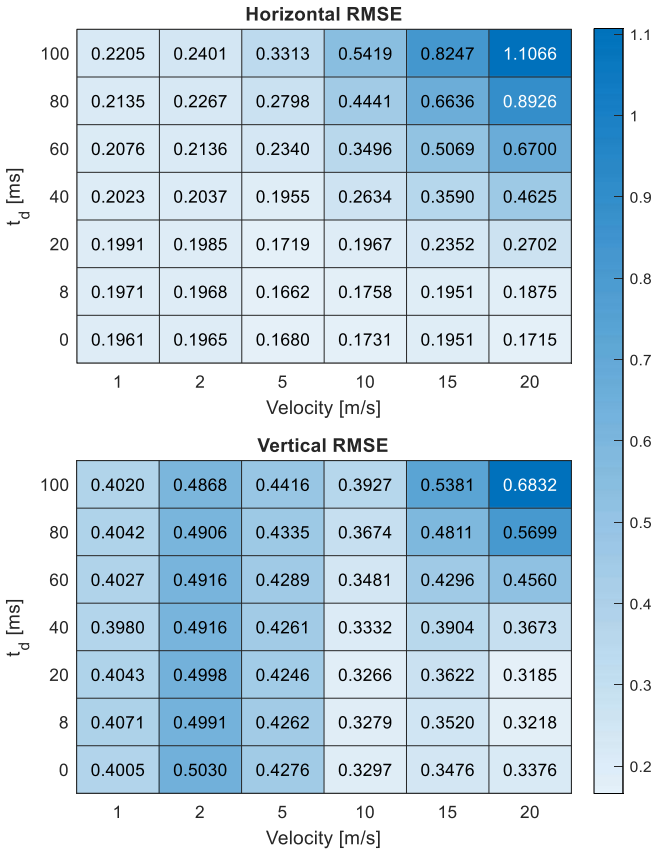

Fig. 5: Heatmap chart of the horizontal and vertical positioning RMSEs in East North Up (ENU) coordinates under uncalibrated GNSS/UWB tight integration. The horizontal axis shows different receiver average speeds. The vertical axis represents different values of t_d. RMSE is expressed in units of metre.

Table II specifies the percentage proportion of horizontal RMSE contributed by uncalibrated t_d to errors contributed by other sources. For simulations in low kinematics, t_d marginally contributes to the measured RMSE. For instance, for a large t_d of $100\,\mathrm{ms}$, the RMSE increase amounts to only $12.44\,\%$ at $1\,\mathrm{m/s}$ average speed. However, when the average receiver velocity increases to $20\,\mathrm{m/s}$, the measured horizontal RMSE enhancement due to uncalibrated t_d grows up to $545.37\,\%$.

C. Enhanced double-update EKF error statistics

In this section, with the aim of pursuing a state-estimation performance analysis in terms of both positioning error statistics and time-calibration accuracy, the simulated GNSS dataset for $20\,\mathrm{m/s}$ average receiver speed is post-processed with a UWB ranging dataset affected by nominal $t_d = 40\,\mathrm{ms}$. In fact, under these operating conditions, a remarkable positioning accuracy degradation has been measured for uncalibrated tight integration according to Table II.

1) Positioning statistics and time-calibration performance: In Fig. 7, the time-series of t_d estimates are outlined for both EKF with naive t_d calibration and double-update EKF. In addition, RMSEs of t_d estimates are summarised in Table III for the considered time-calibration architectures. Apparently, the double-update EKF architecture delivers a smoother t_d estimate (i.e., with lower variance) compared to the results

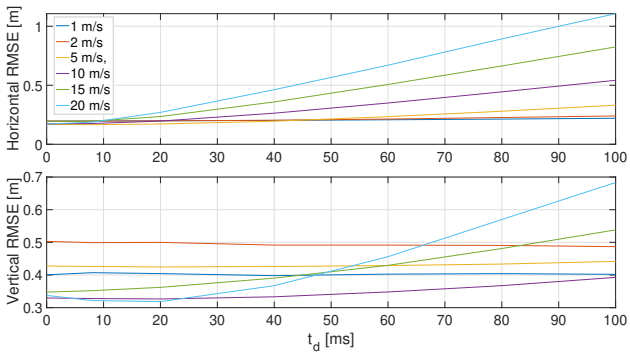

Fig. 6: Trend of the RMSE on the horizontal and vertical positions in ENU-coordinates for different values of t_d. Error curves are parameterised by the receiver average speed.

TABLE II: Percentage increment of the horizontal positioning RMSE contributed by uncalibrated t_d.

t_d [ms]	Average Receiver Speed [m/s]					
	1	2	5	10	15	20
8	0.51	0.15	-1.07	1.56	0.00	9.33
20	1.53	1.02	2.32	13.63	20.55	57.56
40	3.16	3.66	16.37	52.17	84.01	169.68
60	5.86	8.70	39.29	101.96	159.82	290.67
80	8.87	15.37	66.55	156.56	240.13	420.47
100	12.44	22.19	97.20	213.06	322.71	545.48

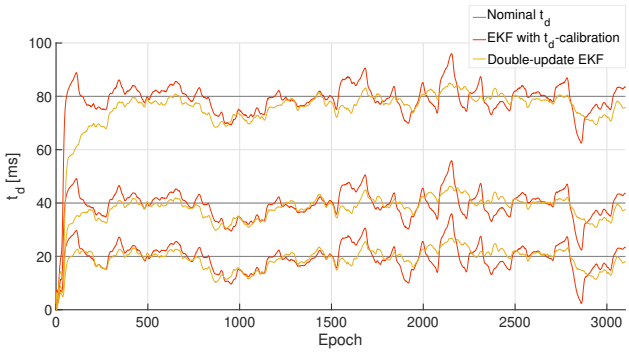

Fig. 7: Time-series of estimated t_d for the simulated trajectory at $20\,\mathrm{m/s}$ average receiver speed. Comparison between EKF with naive t_d calibration and double-update EKF. Nominal t_d values of $20\,\mathrm{ms}$, $40\,\mathrm{ms}$ and $80\,\mathrm{ms}$ are considered.

TABLE III: Time-offset estimation RMSE [ms] for different nominal t_d values.

Tight integration filter	t_d [ms]		
	20	40	80
EKF with t_d-calibration	4.9031	4.8957	4.9460
Double-update EKF	3.6051	3.8301	4.8610

obtained from the EKF with naive t_d calibration. In particular, according to Table III for nominal $t_d = 40$ ms, the double-update EKF pursues a time-calibration accuracy - in RMSE terms - of $3.83\,\mathrm{ms}$, which is higher than that achieved by the EKF with naive t_d calibration (i.e., $4.90\,\mathrm{ms}$) and which translates into a RMSE improvement of $21.77\,\%$.

Fig. 8 highlights the time-series of the positioning error in both the horizontal and the vertical directions. From a general standpoint, both filtering architectures implementing t_d calibration substantially improve horizontal RMSE statistics compared to a plain EKF tight integration, although the vertical gain is moderate due to the poor UWB geometry. More in depth, accounting for the horizontal positioning accuracy in RMSE terms, the EKF with naive t_d calibration reduces the error from $0.46\,\mathrm{m}$ to $0.26\,\mathrm{m}$ compared to a plain EKF integration, and a further higher error reduction down to $0.18\,\mathrm{m}$ is obtained through the double-update EKF scheme.

Further, Fig. 9 illustrates the Empirical Cumulative Density Functions (ECDFs) of the horizontal and the vertical positioning errors in ENU coordinates. What's more, Table IV summarises the horizontal error statistics at few percentiles of interest. At the 50-th percentile, the double-update EKF achieves an average horizontal accuracy gain of $69.80\,\%$ over the plain EKF and of $33.73\,\%$ over the EKF with naive t_d calibration. At the 95-th percentile, instead, the measured horizontal accuracy gains amount to $41.60\,\%$ and $15.43\,\%$, respectively.

Eventually, Table V reports the execution times of involved filtering architectures based on a laptop with Intel i7-10750H (2.6 GHz) processor and 16 GB memory. The EKF with naive t_d calibration keeps almost the same computational complexity

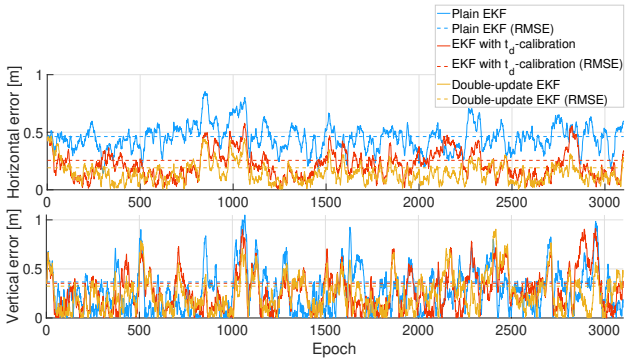

Fig. 8: Horizontal (top) and vertical (bottom) position error trend in ENU-coordinates. Comparison between plain EKF, EKF with naive t_d calibration and double-update EKF. For each architecture, horizontal and vertical RMSE levels are highlighted.

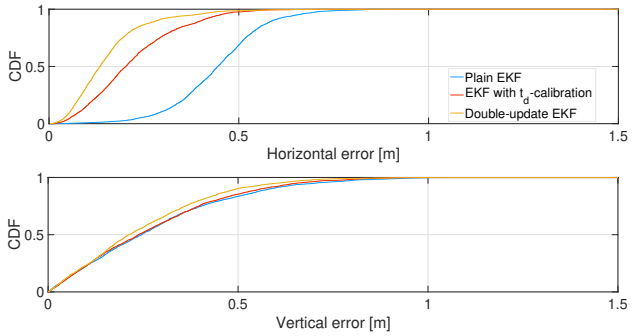

Fig. 9: Empirical CDF (ECDF) lines of the horizontal (top) and vertical (bottom) positioning errors in ENU-coordinates. Comparison between plain EKF, EKF with naive t_d calibration and double-update EKF.

TABLE IV: Evaluation of horizontal positioning errors [m] for the different EKF architectures considering $310\,\mathrm{s}$ (3102 epochs) of PVT computation.

Tight integration filter	Error Percentile [m]		
	50-th	75-th	95-th
Plain EKF (uncalibrated)	0.4443	0.5174	0.6524
EKF with t_d-calibration	0.2025	0.2925	0.4505
Double-update EKF	0.1342	0.1946	0.3810

as the plain EKF. The proposed double-update EKF increases $34.46\,\%$ execution time compared to the plain EKF.

2) Horizontal error statistics for different values of t_d*:* To further assess the proposed EKF-based architectures implementing t_d calibration, multiple UWB ranging datasets are tightly integrated for different nominal t_d values: $20\,\mathrm{ms}$, $40\,\mathrm{ms}$ and $80\,\mathrm{ms}$. Looking back at the time-series of the estimated t_d in Fig. 7, the double-update EKF always pursues higher time-calibration accuracy than the EKF with naive t_d calibration, and the delivered t_d estimates have smaller variance. In particular, according to Table III, the double-update EKF achieves

TABLE V: Program execution time for the different EKF architectures considering 310 s (3102 epochs) of PVT computation.

Tight integration filter	Program execution time $[s]$
Plain EKF (uncalibrated)	18.949
EKF with t_d-calibration	19.113
Double-update EKF	25.479

RMSE accuracy gains of 26.33 % and 1.81 % for nominal t_d values of 20 ms and 80 ms, respectively.

Table VI summarises the horizontal positioning RMSEs in units of metre. As it can be seen, the RMSE for a tight integration via the plain EKF almost doubles for doubling t_d, given fixed average receiver speed. Besides, for $t_d = 20$ ms, the double-update EKF pursues an average horizontal accuracy gain of 26.79 % RMSE over the EKF with naive t_d calibration. Furthermore, for a larger $t_d = 80$ ms, the horizontal gain achieved by the double-update EKF amounts to 14.41 %. Globally, with the increase of t_d, the double-update EKF positioning accuracy improvement drops slightly, and measured RMSEs are close to 0.20 m.

Eventually, horizontal summary statistics can be observed in Fig. 10 in terms of error mean, spread and skewness characterising the positioning estimates delivered by the analysed filters. The superior performance of the proposed double-update EKF algorithm is hence assessed with respect to the other solutions.

3) Horizontal error statistics for varying UWB ranging accuracy: From Section IV, the underlying principle of t_d calibration involves the identification of the misalignment between the position information mapped by GNSS and UWB ranging observables by leveraging the system dynamic model. Therefore, the higher the UWB ranging accuracy is, the more accurate the identification of positions' misalignment should be. In turn, t_d estimation accuracy is expected to improve.

To test the impact of UWB ranging accuracy degradation on tight integration performance, synthetic UWB datasets with amplified UWB ranging measurements' noise standard deviation are generated for integer scaling factors equal to 1 (i.e., no amplification), 2 and 4. In the analysis, the simulated kinematic scenario at 20 m/s average receiver speed is considered under fixed $t_d = 40$ ms. Table VII collects the horizontal positioning RMSEs in units of metre. By cross-comparing the measured RMSEs at $t_d = 40$ ms in Table VI, the accuracy performance of both the EKF with naive t_d calibration and the double-update EKF drops when the UWB ranging accuracy deteriorates. However, the double-update EKF still guarantees superior positioning accuracy performance for any degree of UWB ranging accuracy.

D. Real-world test

To validate the performance of the proposed filtering-based calibration methodology for GNSS/UWB tight integration, a real-world experiment has been carried out about a car ride in a suburban area of the Metropolitan city of Turin (Italy). The maximum achieved average vehicle speed is about 10 m/s. Fig. 11 provides a snapshot of the considered scenario. Although the chosen experimental environment is not expected to severely degrade the quality of GNSS observables, the results of the following analysis are still valuable. In fact, the primary goal of this section is not just validating GNSS/UWB tight integration per se, but rather to emphasize the accuracy improvements GNSS/UWB tight integration can benefit from embedding the proposed time calibration strategy. Furthermore, good GNSS conditions would even be a worst case for GNSS/UWB tight integration because auxiliary UWB measurements might not bring remarkable accuracy gains.

A u-blox ZED-F9P high-precision module has been leveraged which integrates multi-band GNSS and Real-Time Kinematic (RTK) technology [53]. Such positioning module is commonly used in the industrial navigation and robotics markets. In addition, a high-gain, multi-band SinoGNSS AT340 geodetic antenna has been deployed [54]. GNSS noisy pseudorange and Doppler-shift measurements have been logged through the u-blox module for the GPS constellation at 10 Hz rate. In parallel, the multi-band RTK solution from the high-precision GNSS module has been retrieved in order to grant a

TABLE VI: Horizontal positioning RMSE [m] for different nominal t_d.

Tight integration filter	t_d [ms]		
	20	40	80
Plain EKF (uncalibrated)	0.2702	0.4625	0.8926
EKF with t_d-calibration	0.2503	0.2557	0.2755
Double-update EKF	0.1828	0.1931	0.2358

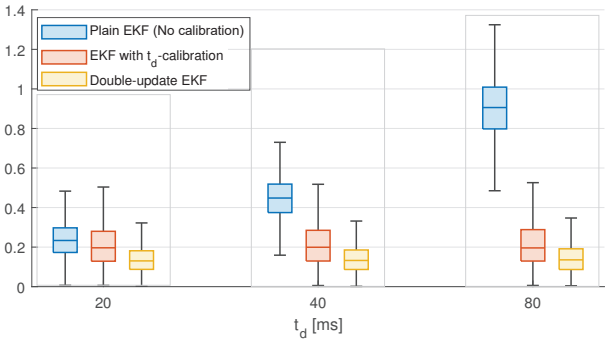

Fig. 10: Box plot of the horizontal positioning error statistics for nominal t_d values of 20 ms, 40 ms and 80 ms.

TABLE VII: Horizontal RMSE [m] for different UWB ranging accuracy

Tight integration filter	Multiplied times of ranging errors' standard deviation		
	1	2	4
Plain EKF (uncalibrated)	0.4625	0.4583	0.4615
EKF with t_d-calibration	0.2557	0.3257	0.4283
Double-update EKF	0.1931	0.2330	0.2948

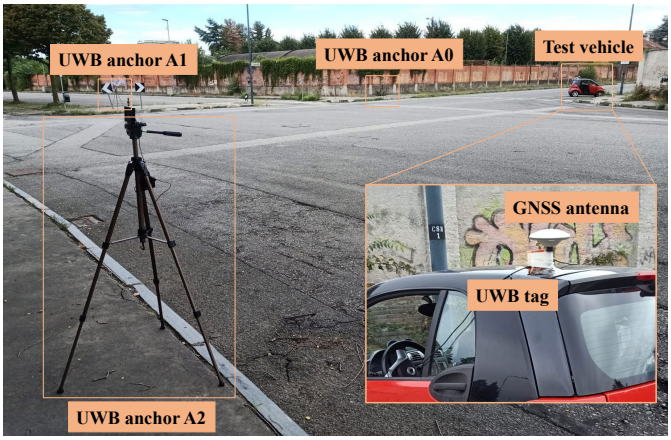

Fig. 11: Snapshot of the experimental scenario for the real-world test campaign. The deployed network of static UWB anchors is shown. Moreover, the UWB tag and the GNSS antenna on the road vehicle's roof are highlighted.

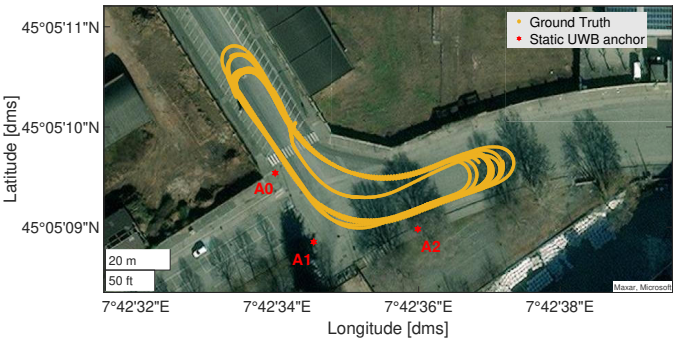

Fig. 12: Map view of the ground reference for the real-world dataset used in the validation of the proposed online time calibration method for GNSS/UWB tight integration.

ground truth (i.e., reference trajectory) useful for the estimation of the error statistics in the tightly integrated navigation solution. The ground-truth path for the tested trajectory is shown in Fig. 12.

On the UWB side, consumer EVB1000 boards from Qorvo Inc. have been employed [55]. In particular, three UWB modules have been installed on tripods as static anchors and their positions have been estimated at sub-decimetre level accuracy. In addition, a fourth UWB module has been operated as tag and installed on the road vehicle's roof. The deployement of both the UWB tag and the GNSS antenna on the vehicle are further highlighted in Fig. 11. As a remark, efforts have been made to minimise the lever arm between the phase centres of the GNSS and the UWB antennas. UWB measurements to the network of static anchors have been logged through the EVB1000 tag module at $5\,\mathrm{Hz}$ rate. When the UWB tag forwards a new measurement to the laptop via the serial port, the Universal Time Coordinated (UTC) time from the laptop is recorded as the timestamp of the corresponding UWB measurement. Besides, a time-offset of $100\,\mathrm{ms}$ is intentionally added to each measurement sample in the UWB dataset in order to enhance the magnitude of GNSS/UWB time-offset. Nonetheless, being added to all the UWB measurement samples by the same amount, it does not undermine the methodology assessment. Furthermore, due to the inaccuracies and non-idealities of the laptop's clock as well as the transmission delays affecting UWB measurements, it has not been possible to retrieve the ground-truth for the GNSS/UWB time-offset. Anyhow, the proposed time-calibration techniques can still be validated by assessing positioning error statistics w.r.t. to the ground truth.

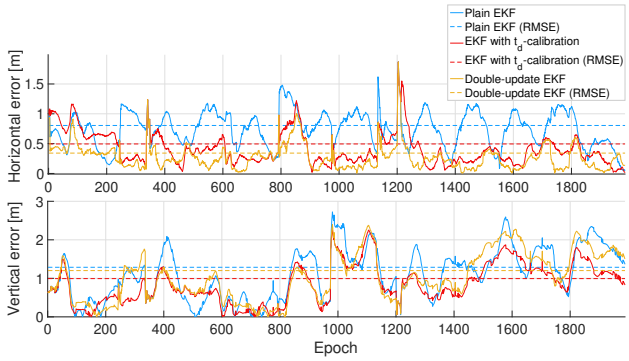

Fig. 13: Horizontal (top) and vertical (bottom) position error trend in ENU-coordinates for the real-world dataset. Comparison between plain EKF, EKF with naive t_d calibration and double-update EKF.

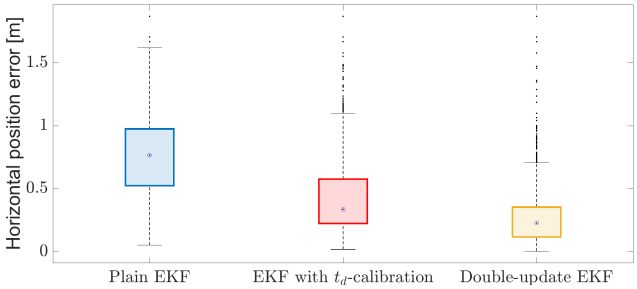

Fig. 14: Box plot of the horizontal positioning error statistics in ENU-coordinates for the real-world dataset. Comparison between plain EKF, EKF with naive t_d calibration and double-update EKF.

TABLE VIII: Horizontal positioning RMSE $[\mathrm{m}]$ for different t_d calibration architectures in the real-world test.

Tight integration filter	Horizontal positioning RMSE $[m]$
Plain EKF (uncalibrated)	0.8043
EKF with t_d-calibration	0.4947
Double-update EKF	0.3412

Fig. 13 shows the positioning error time-series both for the horizontal and vertical components in local ENU frame. As a matter of fact, vertical statistics are penalised by the geometry of the deployed network of UWB anchors. In addition, the vertical component of the vehicle speed approaches zero for most of the trajectory course. Focusing on the horizontal component, Table VIII summarises the positioning RMSEs in units of metre. The double-update EKF achieves horizontal RMSE improvements of $31.03\,\%$ and $57.58\,\%$ compared to the EKF

with naive t_d calibration and the uncalibrated tight integration via plain EKF, respectively. Eventually, horizontal summary statistics for the real-world dataset are highlighted in Fig. 14 in terms of error mean, spread and skewness characterising the positioning estimates delivered by the analysed filters. At the 75-th percentile, the double-update EKF achieves horizontal gains of $38.54\,\%$ over the EKF with naive t_d calibration and of $63.67\,\%$ over the plain EKF. As such, a globally exhaustive evidence of the superior performance of the proposed double-update EKF algorithm for online GNSS/UWB time-calibration is given. It is worth noticing that the conditions of the experimental environment (i.e., few UWB anchors while generous open sky visibility of GNSS satellites) do not limit the validity of the test. The scenario is suboptimal in terms of maximum achievable accuracy of a tight GNSS/UWB architecture, but it shows the benefits introduced by the proposed time calibration technique.

VI. Conclusions

Time calibration is of great concern in GNSS/UWB tight integration leveraging centralised EKF hybridisation, and this paper has explored the impact of uncalibrated GNSS/UWB time-offset on state-estimation accuracy both theoretically and experimentally. Based on these premises, an EKF-based framework has been proposed to address time-offset calibration. First, an improved GNSS/UWB tight integration model has been presented to enable the modelling of the unknown time-offset as part of the EKF-based state-space formulation. Then, after pointing out criticalities in time-offset estimation owing to local losses of identifiability, an enhanced, double-update EKF architecture has been put forward which adaptively weights UWB covariance statistics. Simulation results demonstrate that, under challenging kinematic conditions causing remarkable accuracy deterioration for uncalibrated GNSS/UWB tight integration, the EKF with naive time-offset calibration can reduce the horizontal positioning RMSE from $0.4625\,\mathrm{m}$ to $0.2557\,\mathrm{m}$, while the double-update EKF with statistical modelling optimisations can achieve higher RMSE reduction down to $0.1931\,\mathrm{m}$. Moreover, results obtained with a real-world dataset further assess the superior double-update EKF performance by highlighting horizontal gains of $57.58\,\%$ compared to the uncalibrated tight integration via plain EKF and of $31.03\,\%$ over the EKF with naive time-offset calibration.

References

[1] Y. J. Morton, F. van Diggelen, J. James J. Spilker, and B. W. Parkinson, "Position, Navigation, and Timing for Consumer and Commercial Applications," in *Position, Navigation, and Timing Technologies in the 21st Century: Integrated Satellite Navigation, Sensor Systems, and Civil Applications*. John Wiley & Sons, Inc., December 2020, vol. 2, pp. 1711–1970.

[2] D. Perea-Strom, A. Morell, J. Toledo, and L. Acosta, "GNSS integration in the localization system of an autonomous vehicle based on particle weighting," *IEEE Sensors Journal*, vol. 20, no. 6, pp. 3314–3323, 2019.

[3] C. Cristodaro, F. Dovis, G. Falco, and M. Pini, "GNSS receiver performance in urban environment: Challenges and test approaches for automotive applications," in *2017 International Conference of Electrical and Electronic Technologies for Automotive*, 2017, pp. 1–6.

[4] K.-W. Chiang, H.-W. Chang, Y.-H. Li, G.-J. Tsai, C.-L. Tseng, Y.-C. Tien, and P.-C. Hsu, "Assessment for ins/gnss/odometer/barometer integration in loosely-coupled and tightly-coupled scheme in a gnss-degraded environment," *IEEE Sensors Journal*, vol. 20, no. 6, pp. 3057–3069, 2019.

[5] L.-T. Hsu, Y. Gu, Y. Huang, and S. Kamijo, "Urban pedestrian navigation using smartphone-based dead reckoning and 3-d map-aided gnss," *IEEE Sensors Journal*, vol. 16, no. 5, pp. 1281–1293, 2015.

[6] C. Cristodaro, "Advanced Integration of GNSS and External Sensors for Autonomous Mobility Applications," Ph.D. dissertation, ScuDo, Politecnico di Torino, Turin, Italy, May 2019, prof. F. Dovis, Supervisor. [Online]. Available: http://hdl.handle.net/11583/2734313

[7] L. Chang, X. Niu, T. Liu, J. Tang, and C. Qian, "GNSS/INS/LiDAR-SLAM Integrated Navigation System Based on Graph ," *Remote Sensing*, vol. 11, no. 9, 2019. [Online]. Available: https://www.mdpi.com/2072-4292/11/9/1009

[8] R. Zekavat and R. M. Buehrer, "Wireless Localization Using Ultra-Wideband Signals," in *Handbook of Position Location: Theory, Practice, and Advances*. Wiley-IEEE Press, 2019, pp. 269–301.

[9] Q. Tian, I. Kevin, K. Wang, and Z. Salcic, "A low-cost ins and uwb fusion pedestrian tracking system," *IEEE Sensors Journal*, vol. 19, no. 10, pp. 3733–3740, 2019.

[10] Z. Sahinoglu, S. Gezici, and I. Güvenc, *Ultra-wideband Positioning Systems: Theoretical Limits, Ranging Algorithms, and Protocols*. Cambridge University Press, 2008.

[11] J. N. Gross, Y. Gu, and B. Dewberry, "Tightly-Coupled GPS/UWB-Ranging for Relative Navigation During Formation Flight," in *Proceedings of the 27th International Technical Meeting of the Satellite Division of The Institute of Navigation (ION GNSS+ 2014)*, September 2014, pp. 1698–1708.

[12] M. Arulampalam, S. Maskell, N. Gordon, and T. Clapp, "A tutorial on particle filters for online nonlinear/non-Gaussian Bayesian tracking," *IEEE Transactions on Signal Processing*, vol. 50, no. 2, pp. 174–188, 2002. [Online]. Available: https://doi.org/10.1109/78.978374

[13] O. Vouch, A. Minetto, G. Falco, and F. Dovis, "On the Adaptivity of Unscented Particle Filter for GNSS/INS Tightly-Integrated Navigation Unit in Urban Environment," *IEEE Access*, vol. 9, pp. 144 157–144 170, 2021.

[14] S. Julier and J. Uhlmann, "Fusion of time delayed measurements with uncertain time delays," in *Proceedings of the 2005, American Control Conference, 2005.*, 2005, pp. 4028–4033 vol. 6.

[15] I. Skog and P. Handel, "Time Synchronization Errors in Loosely Coupled GPS-Aided Inertial Navigation Systems," *IEEE Transactions on Intelligent Transportation Systems*, vol. 12, no. 4, pp. 1014–1023, 2011.

[16] T. Qin and S. Shen, "Online temporal calibration for monocular visual-inertial systems," in *2018 IEEE/RSJ International Conference on Intelligent Robots and Systems (IROS)*, 2018, pp. 3662–3669.

[17] H. K. Lee, J. G. Lee, and G.-I. Jee, "Calibration of time synchronization error in gps/sdins hybrid navigation," *IFAC Proceedings Volumes*, vol. 34, no. 15, pp. 223–228, 2001, 15th IFAC Symposium on Automatic Control in Aerospace, Bologna/Forlì, Italy, September 2-7, 2001. [Online]. Available: https://www.sciencedirect.com/science/article/pii/S1474667017407312

[18] W. Ding, J. Wang, Y. Li, P. Mumford, and C. Rizos, "Time Synchronization Error and Calibration in Integrated GPS/INS Systems," *ETRI Journal*, vol. 30, no. 1, pp. 59–67, 2008. [Online]. Available: https://onlinelibrary.wiley.com/doi/abs/10.4218/etrij.08.0106.0306

[19] W. Ding, J. Wang, P. Mumford, Y. Li, and C. Rizos, "Time synchronization design for integrated positioning and georeferencing systems," in *Proceedings of SSC*, 2005, pp. 1265–1274.

[20] G. Du, L. Wang, C. Zhai, and X. Zhan, "A Flexible Low-cost Time Synchronizer for GNSS/INS Integration," in *Proceedings of the 23rd International Technical Meeting of the Satellite Division of The Institute of Navigation (ION GNSS 2010)*, 2010, pp. 2100–2105.

[21] J. Kelly and G. S. Sukhatme, *A General Framework for Temporal Calibration of Multiple Proprioceptive and Exteroceptive Sensors*. Berlin, Heidelberg: Springer Berlin Heidelberg, 2014, pp. 195–209.

[22] J.-O. Nilsson, I. Skog, and P. Händel, "Joint state and measurement time-delay estimation of nonlinear state space systems," in *10th International Conference on Information Science, Signal Processing and their Applications (ISSPA 2010)*. IEEE, 2010, pp. 324–328.

[23] J. Rehder, R. Siegwart, and P. Furgale, "A General Approach to Spatiotemporal Calibration in Multisensor Systems," *IEEE Transactions on Robotics*, vol. 32, no. 2, pp. 383–398, 2016.

[24] M. Huber, M. Schlegel, and G. Klinker, "Temporal calibration in multisensor tracking setups," in *2009 8th IEEE International Symposium on Mixed and Augmented Reality*, 2009, pp. 195–196.

[25] J. Nikolic, M. Burri, I. Gilitschenski, J. Nieto, and R. Siegwart, "Non-parametric extrinsic and intrinsic calibration of visual-inertial sensor systems," *IEEE Sensors Journal*, vol. 16, no. 13, pp. 5433–5443, 2016.

[26] J. Kelly, N. Roy, and G. S. Sukhatme, "Determining the time delay between inertial and visual sensor measurements," *IEEE Transactions on Robotics*, vol. 30, no. 6, pp. 1514–1523, 2014.

[27] R. Voges and B. Wagner, "Timestamp offset calibration for an imu-camera system under interval uncertainty," in *2018 IEEE/RSJ International Conference on Intelligent Robots and Systems (IROS)*, 2018, pp. 377–384.

[28] W. Huang, W. Wan, and H. Liu, "Optimization-based online initialization and calibration of monocular visual-inertial odometry considering spatial-temporal constraints," *Sensors*, vol. 21, no. 8, 2021. [Online]. Available: https://www.mdpi.com/1424-8220/21/8/2673

[29] J. Peršić, L. Petrović, I. Marković, and I. Petrović, "Spatiotemporal multisensor calibration via gaussian processes moving target tracking," *IEEE Transactions on Robotics*, vol. 37, no. 5, pp. 1401–1415, 2021.

[30] J. Kelly, C. Grebe, and M. Giamou, "A question of time: Revisiting the use of recursive filtering for temporal calibration of multisensor systems," in *2021 IEEE International Conference on Multisensor Fusion and Integration for Intelligent Systems (MFI)*, 2021, pp. 1–8.

[31] M. Li and A. I. Mourikis, "3-d motion estimation and online temporal calibration for camera-imu systems," in *2013 IEEE International Conference on Robotics and Automation*, 2013, pp. 5709–5716.

[32] A. Goudar and A. P. Schoellig, "Online Spatio-temporal Calibration of Tightly-coupled Ultrawideband-aided Inertial Localization," in *2021 IEEE/RSJ International Conference on Intelligent Robots and Systems (IROS)*, 2021, pp. 1161–1168.

[33] M. Grewal and K. Glover, "Identifiability of linear and nonlinear dynamical systems," *IEEE Transactions on Automatic Control*, vol. 21, no. 6, pp. 833–837, 1976.

[34] R. Griffin and A. Sage, "Sensitivity analysis of discrete filtering and smoothing algorithms," *AIAA Journal*, vol. 7, no. 10, pp. 1890–1897, October 1969. [Online]. Available: https://doi.org/10.2514/3.5477

[35] P. W. Ward, J. W. Betz, and C. J. Hegarty, "Performance of Stand-Alone GPS," in *Understanding GPS: Principles and Applications*, 2nd ed., E. Kaplan and C. J. Hegarty, Eds. 685 Canton Street Norwood, MA 02062: Artech House, Inc., 2006, ch. 7, pp. 301–378.

[36] P. Misra and P. Enge, *Global Positioning System: Signals, Measurements, and Performance*, 2nd ed. Ganga-Jamuna Press, December 2010.

[37] J. Yan, C. C. J. M. Tiberius, G. J. M. Janssen, P. J. G. Teunissen, and G. Bellusci, "Review of range-based positioning algorithms," *IEEE Aerospace and Electronic Systems Magazine*, vol. 28, no. 8, pp. 2–27, 2013.

[38] D. Dardari, A. Conti, U. Ferner, A. Giorgetti, and M. Z. Win, "Ranging with ultrawide bandwidth signals in multipath environments," *Proceedings of the IEEE*, vol. 97, no. 2, pp. 404–426, 2009.

[39] K. Li, B. Hu, L. Chang, and Y. Li, "Comparison of direct navigation mode and indirect navigation mode for integrated SINS/GPS," *Transactions of the Institute of Measurement and Control*, vol. 38, no. 1, pp. 3–13, 2016. [Online]. Available: https://doi.org/10.1177/0142331214568236

[40] P. Groves, *Principles of GNSS, Inertial, and Multisensor Integrated Navigation Systems*, 2nd ed. 16 Sussex Street, London: Artech House, 2013.

[41] R. G. Brown and P. Y. Hwang, "Introduction to random signals and applied kalman filtering(book)," *New York, John Wiley & Sons, Inc., 1992. 512*, 1992.

[42] M. Caceres Duran, P. Closas, E. Falletti, C. Fernández-Prades, M. Nájar, and F. Sottile, "Signal Processing for Hybridization," in *Satellite and Terrestrial Radio Positioning Technique*, D. Dardari, E. Falletti, and M. Luise, Eds. Oxford: Academic Press, 2012, ch. 6, pp. 317–382. [Online]. Available: https://doi.org/10.1016/B978-0-12-382084-6.00006-4

[43] P. C. Gomez, "Bayesian Signal Processing Techniques for GNSS Receivers: from multipath mitigation to positioning," Ph.D. dissertation, Universitat Politecnica de Catalunya, Department of Signal Theory and Communications, Barcelona, Spain, June 2009, prof. A. Fernandez Rubio, Supervisor.

[44] Y. Bar-Shalom, X. R. Li, and T. Kirubarajan, *Estimation with applications to tracking and navigation: theory algorithms and software*. John Wiley & Sons, 2004.

[45] F. Gustafsson, F. Gunnarsson, N. Bergman, U. Forssell, J. Jansson, R. Karlsson, and P.-J. Nordlund, "Particle filters for positioning, navigation, and tracking," *IEEE Transactions on Signal Processing*, vol. 50, no. 2, pp. 425–437, 2002.

[46] H. Yiğitler, B. Badihi, and R. Jäntti, "Overview of time synchronization for IoT deployments: Clock discipline algorithms and protocols," *Sensors*, vol. 20, no. 20, p. 5928, 2020.

[47] M. Win and R. Scholtz, "On the robustness of ultra-wide bandwidth signals in dense multipath environments," *IEEE Communications Letters*, vol. 2, no. 2, pp. 51–53, 1998.

[48] D. Dardari, A. Conti, U. Ferner, A. Giorgetti, and M. Z. Win, "Ranging With Ultrawide Bandwidth Signals in Multipath Environments," *Proceedings of the IEEE*, vol. 97, no. 2, pp. 404–426, 2009.

[49] W. M. Gifford, D. Dardari, and M. Z. Win, "The Impact of Multipath Information on Time-of-Arrival Estimation," *IEEE Transactions on Signal Processing*, vol. 70, pp. 31–46, 2022.

[50] H. Kuusniemi, "User-level reliability and quality monitoring in satellite-based personal navigation," Ph.D. dissertation, Tampere University of Technology, Tampere, Finland, 2005, prof. J. Takala and Prof. G. Lachapelle, Supervisors.

[51] R. Zekavat and R. M. Buehrer, *Impact of Anchor Placement and Anchor Selection on Localization Accuracy*. Wiley-IEEE Press, 2019, pp. 435–465.

[52] G. Fantin, "UWB localization system for partially GPS-denied robotic applications," April 2019, unpublished, available in the archive. [Online]. Available: http://webthesis.biblio.polito.it/10888/

[53] u-blox Holding AG, "Zed-f9p-04b data sheet," 5 2022, [online]. [Online]. Available: https://www.u-blox.com/en/product/zed-f9p-module

[54] ComNav Technology Ltd., "Sinognss at340 geodetic antenna data sheet," 11 2020, [online]. [Online]. Available: https://www.comnavtech.com/AT340.html

[55] Qorvo Inc., "DecaWave EVB1000 Data Sheet," 11 2020, [online].

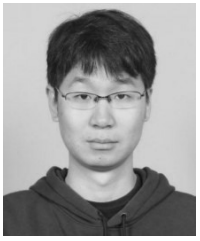

Yihan Guo received the B.Sc. degree from Northwestern Polytechnical University (Xi'an, Shaanxi, China) in 2016, and the M.Sc. degree from Shanghai Jiaotong University (Shanghai, China) in 2019. He is a Ph.D. student at the Department of Electronics and Telecommunications (DET) of Politecnico di Torino (Turin, Italy) and member of the Navigation Signal Analysis and Simulation - NavSAS - group. His current research interests include integrated navigation systems based on Global Navigation Satellite System (GNSS) and Ultra-Wideband (UWB).

Oliviero Vouch received the B.Sc. degree in Electronics and Communications Engineering (ECE) in 2018 and the M.Sc. degree in Communications and Computer Networks Engineering (CCNE) in 2020, both from Politecnico di Torino (Turin, Italy). He joined the Department of Electronics and Telecommunications (DET) of Politecnico di Torino as a Ph.D. student in 2021 and he is member of the Navigation Signal Analysis and Simulation - NavSAS - group. His academic background includes advanced signal processing and his current research interests cover advanced Bayesian estimation applied to multi-sensor integrated navigation units based on Global Navigation Satellite System (GNSS).

Simone Zocca received a B.Sc. in Telecommunication Engineering in 2018 and a M.Sc. in Communication and Computer Networks Engineering in 2020, both from Politecnico di Torino (Turin, Italy). He is currently a Ph.D. student within the Navigation Signal Analysis and Simulation - NavSAS - group at the Department of Electronics and Telecommunications (DET) of Politecnico di Torino. His research is focused on innovative solutions for signal processing techniques and Bayesian estimation applied to Global Navigation Satellite System (GNSS).

Alex Minetto (GS'17-M'20) received the B.Sc. and M.sc. degrees in Telecommunications Engineering from Politecnico di Torino (Turin, Italy) and his Ph.D. degree in Electrical, Electronics and Communications Engineering (EECE), in 2020. He joined the Department of Electronics and Telecommunications (DET) of Politecnico di Torino in 2019 as research and teaching assistant. In 2015 he spent a six-month internship at European Organisation for the Exploitation of Metereological Satellites (EUMETSAT, Darmstadt, Germany). His current research interests cover signal processing and advanced Bayesian estimation applied to Global Navigation Satellite System (GNSS) cooperative receivers.

Fabio Dovis (GS'98-M'01) Fabio Dovis (Member, IEEE) received the M.Sc. and Ph.D. degrees from the Politecnico di Torino, Turin, Italy, in 1996 and 2000, respectively. In 2004, he joined the Department of Electronics and Telecommunications, where he has been a Full Professor since 2021. He coordinates the Navigation, Signal Analysis and Simulation Research Group (NavSAS). His research addresses the design of Global Navigation Satellite System (GNSS) receivers, and advanced signal processing for GNSS impairments. He authored more than 70 journal papers and more than 150 papers in conference proceedings. He is a member of the IEEE Aerospace and Electronic Systems Society (AESS) navigation systems panel, and he is currently serving on the Council of the US Institute of Navigation (ION). He is a member of the GNSS Scientific Advisory Committee (GSAC) of the European Space Agency (ESA).